Check for updates

Numerical Investigation of Ultra-High Lift Coefficient Co-Flow Jet Wing Without Flaps

Yunchao Yang [*] Gecheng Zha [†]

Dept. of Mechanical and Aerospace Engineering
University of Miami, Coral Gables, Florida 33124
E-mail: gzha@miami.edu

Abstract

Recent advances in 2D Co-Flow Jet (CFJ) flow control airfoil has achieved the super-lift coefficient that exceeds theoretical lift coefficient limit [1]. The super lift coefficient of the 3D finite-span CFJ wing has not yet been investigated. To understand the aerodynamic performance of the finite-span CFJ wing, numerical simulations were conducted at high angles of attack for the takeoff/landing conditions in this paper. This paper applies the Super-Lift 2D CFJ airfoil to 3D finite span wings to investigate the flapless wing performance and the capability of ultra-high lift coefficient generation for takeoff and landing performance. The 3D wings with aspect ratio of 20, 10 and 5 are studied. The Reynolds averaged Navier-Stokes equations (RANS) are solved with the Spalart-Allmaras (S-A) turbulence model. The fifth-order WENO scheme is used to reconstruct the inviscid fluxes and a fourth-order central differencing scheme is used to reconstruct the viscous fluxes. The simulations are performed at Mach number of 0.063 and Reynolds number of 3.03×10^6. The CFJ wing is generated by the CFJ6421-SST016-SUC053-INJ009 airfoil, which is designed for the super-lift coefficient. The aspect ratio of CFJ wing of 20, 10, and 5 is studied. The simulations are conducted at the AoA of 25°, 45°, and 70° with the CFJ jet momentum coefficient C_μ of 0.15, 0.2, 0.25 and 0.3. The maximum lift coefficient of $C_L = 7.81$ is achieved at AoA = 70°, C_μ=0.3 , and aspect ratio of 20. The lift coefficient of CFJ wing is reduced compared to that of a 2D airfoil, while the drag is increased due to lift induced wingtip vortex. The Oswald efficiency of 3D CFJ wing is much higher than that of the conventional wing with no flow control. It indicates that the penalty of induced drag for 3D CFJ wing is small with decreased aspect ratio even though very high lift coefficient is obtained.

Nomenclature

AR	Aspect Ratio=$\frac{b^2}{S}$
EBF	External Blown Flaps
IBF	Internal Blown Flap
$CESTOL$	Cruise-Efficient Short Takeoff and Landing
$ESTOL$	Extreme Short Take-Off and Landing
AoA	Angle of Attack
AFC	Active Flow Control
CFJ	Co-Flow Jet
$FASIP$	Flow-Acoustics-Structure Interaction Package
LE	Leading Edge

---

[*] Ph.D. Candidate, AIAA student member
[†] Professor, ASME Fellow, AIAA associate Fellow

Approved for public release; distribution is unlimited.

TE	Trailing Edge
$RANS$	Reynolds-Averaged Navier-Stokes
$ZNMF$	Zero-Net Mass Flux
P	CFJ pumping power consumption, $P = \frac{\dot{m}C_p T_{t2}}{\eta}(\Gamma^{\frac{\gamma-1}{\gamma}} - 1)$
η	CFJ pumping system efficiency, propeller efficiency
P_c	Power coefficient, $P_c = \frac{P}{\frac{1}{2}\rho_\infty V_\infty^3 S}$
PR	Total pressure ratio, Γ
C_L	Lift coefficient
C_D	Drag coefficient
C_M	Moment coefficient
C_μ	Jet momentum coefficient, $C_\mu = \frac{\dot{m}V_j}{\frac{1}{2}\rho_\infty V_\infty^2 S}$
C_{Lmax}	Maximum lift coefficient
$(L/D)_c$	Aerodynamic efficiency corrected for CFJ airfoil, $\frac{L}{D+P/V_\infty}$
C_{RW}	Productivity parameter for a propeller engine airplane
C_L^2/C_D	Productivity efficiency coefficient
$(C_L^2/C_D)_c$	Productivity efficiency coefficient corrected for CFJ airfoil, $(C_L^2/SC_D)_c = C_L^2/(C_D + P_c)$
R	Aircraft range
$\overline{W}$	The averaged weight of the aircraft during cruise
R_e	Reynolds number
M	Mach number
M_{is}	Isentropic Mach number
C_p	Pressure coefficient
c_p	Constant pressure specific heat
γ	Air specific heats ratio
S	Platform area of the wing
ρ_∞	Freestream density
V_∞	Freestream velocity
T_t	Total temperature
P_t	Total pressure
H_t	Total specific enthalpy
α	Angle of attack
$\dot{m}$	Mass flow across the pump
C	Chord length
j	Subscript, stands for jet
c	Subscript, stands for corrected

1   Introduction

Active flow control is considered as one of the most promising technologies to achieve ultra-high cruise efficiency and extremely short take-off and landing for the next generation aircraft. The maximum achievable lift coefficient C_{Lmax} of a wing is critical for aircraft take-off/landing. Achieving high C_{Lmax} is hence crucial to increase future airport capacity and reduce airport community noise. The super-lift coefficient $C_{Lmax} > 2\pi(1+\frac{t}{c})$ is demonstrated by CFD simulation for the 2D Co-Flow Jet (CFJ) flow control [2, 3, 4, 5, 6, 7, 8, 9, 10, ?, 1, 12] in the previous

research, which makes the CFJ flow control very promising to achieve the two features of ultra-high cruise efficiency and extremely short take-off and landing. The CFJ airfoil has great potential to radically change the overall aircraft design philosophy from subsonic to transonic speeds.

The CFJ airfoil has an injection slot near the leading edge (LE) and a suction slot near the trailing edge (TE) on the airfoil upper surface as sketched in Fig. 1. A small amount of mass flow is withdrawn into the airfoil near the TE, pressurized and energized by a pumping system inside the airfoil, and then injected near the LE in the direction tangent to the main flow. The whole process does not add any mass flow to the system and hence is a zero-net mass-flux (ZNMF) flow control. It is a self-contained high lift system with no moving parts.
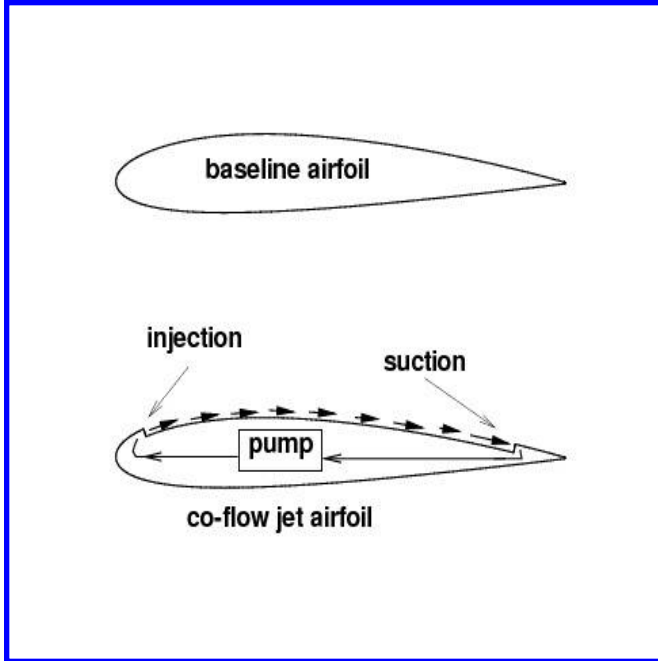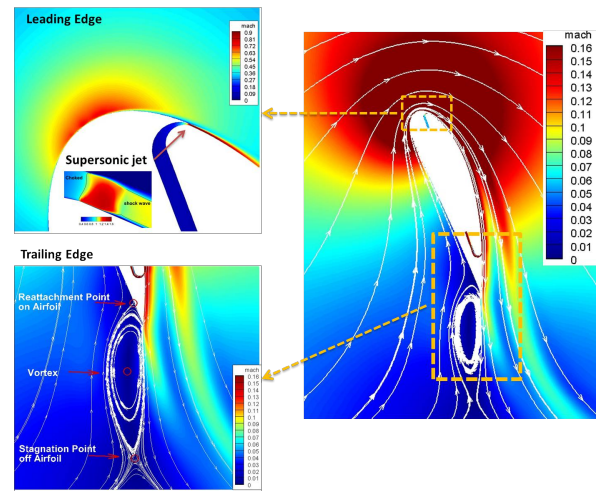

Figure 1: Baseline airfoil and CFJ airfoil.

Figure 2: Mach number contours and streamlines at $C_\mu = 0.35$ and AoA $=70°$ for the CFJ6421-SST016-SUC053-INJ009 airfoil.

The fundamental mechanism of the CFJ airfoil is that the turbulent mixing between the jet and main flow energizes the wall boundary-layer, which dramatically increases the circulation, augmenting lift, and reducing the total drag(or generates thrust) by filling the wake velocity deficit. The CFJ airfoil has a unique low energy expenditure mechanism because the jet gets injected at the leading edge suction peak location, where the main flow pressure is the lowest and makes it easy to eject the flow, and it gets sucked at near the trailing edge, where the main flow pressure is the highest and makes it easy to withdraw the flow. Fig. 2 is the flow structures of a super-lift coefficient CFJ airfoil flow at AoA=70° from 2D RANS simulation conducted by Yang and Zha[1]. A very high circulation generating the super-lift coefficient makes the stagnation point detached from the airfoil. The trailing edge vortex creates an extended virtual solid body to form a high-pressure region due to the stagnant flow to support the airfoil with super-lift coefficient. The high-momentum jet mixes with the free stream and makes the flow attached near the suction surface.

The CFJ airfoil configurations are created from the baseline NACA 6421 airfoil by translating the suction surface downward, which is defined as the suction surface translation (SST). The CFJ injection and suction slot sizes are iterated with trade study to obtain high lift coefficient for take-off and landing, and high aerodynamic efficiency for cruise condition. Fig. 3 shows several CFJ airfoil geometries with SST, injection slot sizes and suction slot sizes. The CFJ6421-SST016-SUC053-INJ009 airfoil is used in this study.
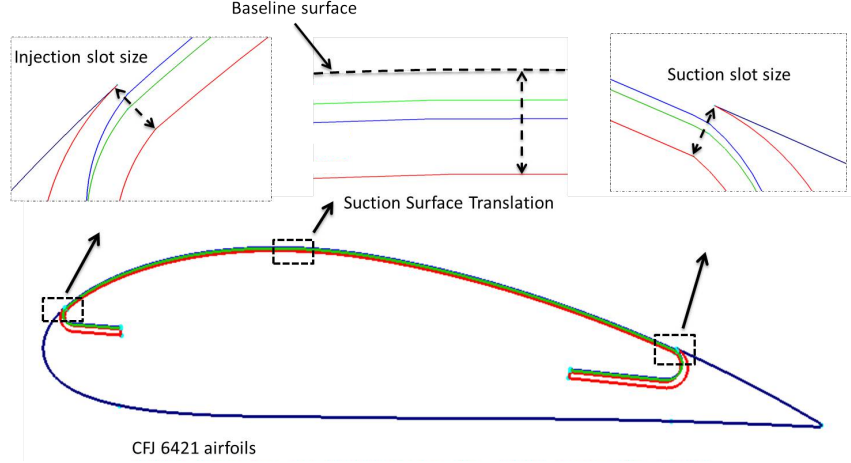
3

Figure 3: CFJ6421 airfoil geometry

In [21](given below) , Lefebvre and Zha studied a 3D CFJ wing at cruise and takeoff/landing performance with the same configuration. The C_{Lmax} achieved in [21] is 4.7. In [1], Yang and Zha indicate that it is beneficial to have larger injection slot size for high cruise efficiency, whereas to achieve Super-Lift coefficient for takeoff/landing, a reduced injection slot size with higher jet speed is more desirable.

The objective of this paper is to apply the Super-Lift 2D CFJ airfoil to 3D finite span wings to investigate the wing performance and the capability of ultra-high lift coefficient generation for takeoff and landing performance without using any flaps. The study is hence focused only on the angle of attack of 25° and higher up to 70°.

2 Numerical Methodology

2.1 Governing Equations

The Reynolds averaged 3D Navier-Stokes governing equations in generalized coordinates are expressed as:

$$\frac{\partial \mathbf{Q}}{\partial t} + \frac{\partial \mathbf{E}}{\partial \xi} + \frac{\partial \mathbf{F}}{\partial \eta} + \frac{\partial \mathbf{G}}{\partial \zeta} = \frac{1}{Re} \left(\frac{\partial \mathbf{E}_v}{\partial \xi} + \frac{\partial \mathbf{F}_v}{\partial \eta} + \frac{\partial \mathbf{G}_v}{\partial \zeta} + \mathbf{S} \right) \tag{1}$$

where Re is the Reynolds number. The equations are nondimenisonalized based on airfoil chord L_∞, freestream density ρ_∞ and velocity U_∞.

The conservative variable vector $\mathbf{Q}$, the inviscid flux vectors $\mathbf{E}$, $\mathbf{F}$, $\mathbf{G}$, the viscous flux $\mathbf{E_v}$, $\mathbf{F_v}$, $\mathbf{G_v}$ and the source term vector $\mathbf{S}$ are expressed as

$$\mathbf{Q} = \frac{1}{J} \begin{pmatrix} \bar{\rho} \\ \bar{\rho}\tilde{u} \\ \bar{\rho}\tilde{v} \\ \bar{\rho}\tilde{w} \\ \bar{\rho}\tilde{e} \\ \bar{\rho}\tilde{\nu}_t \end{pmatrix}, \mathbf{E} = \begin{pmatrix} \bar{\rho}U \\ \bar{\rho}\tilde{u}U + l_x\bar{p} \\ \bar{\rho}\tilde{v}U + l_y\bar{p} \\ \bar{\rho}\tilde{w}U + l_z\bar{p} \\ (\bar{\rho}\tilde{e} + \bar{p})U - l_t\bar{p} \\ \bar{\rho}\tilde{\nu}U \end{pmatrix}, \mathbf{F} = \begin{pmatrix} \bar{\rho}V \\ \bar{\rho}\tilde{u}V + m_x\bar{p} \\ \bar{\rho}\tilde{v}V + m_y\bar{p} \\ \bar{\rho}\tilde{w}V + m_z\bar{p} \\ (\bar{\rho}\tilde{e} + \bar{p})V - m_t\bar{p} \\ \bar{\rho}\tilde{\nu}V \end{pmatrix}, \mathbf{G} = \begin{pmatrix} \bar{\rho}W \\ \bar{\rho}\tilde{u}W + n_x\bar{p} \\ \bar{\rho}\tilde{v}W + n_y\bar{p} \\ \bar{\rho}\tilde{w}W + n_z\bar{p} \\ (\bar{\rho}\tilde{e} + \bar{p})W - n_t\bar{p} \\ \bar{\rho}\tilde{\nu}W \end{pmatrix} \tag{2}$$

4

$$\mathbf{E_v} = \begin{pmatrix} 0 \\ l_k \bar{\tau}_{xk} \\ l_k \bar{\tau}_{yk} \\ l_k \bar{\tau}_{zk} \\ l_k \left(\tilde{u}_i \bar{\tau}_{ki} - \bar{q}_k \right) \\ \frac{\bar{\rho}}{\sigma} \left(\nu + \tilde{\nu} \right) \left(\mathbf{l} \bullet \nabla \tilde{\nu} \right) \end{pmatrix}, \mathbf{F_v} = \begin{pmatrix} 0 \\ m_k \bar{\tau} u_{xk} \\ m_k \bar{\tau}_{yk} \\ m_k \bar{\tau} u_{zk} \\ m_k \left(\tilde{u}_i \bar{\tau}_{ki} - \bar{q}_k \right) \\ \frac{\bar{\rho}}{\sigma} \left(\nu + \tilde{\nu} \right) \left(\mathbf{m} \bullet \nabla \tilde{\nu} \right) \end{pmatrix}, \mathbf{G_v} = \begin{pmatrix} 0 \\ n_k \bar{\tau}_{xk} \\ n_k \bar{\tau}_{yk} \\ n_k \bar{\tau}_{zk} \\ n_k \left(\tilde{u}_i \bar{\tau}_{ki} - \bar{q}_k \right) \\ \frac{\bar{\rho}}{\sigma} \left(\nu + \tilde{\nu} \right) \left(\mathbf{n} \bullet \nabla \tilde{\nu} \right) \end{pmatrix} \tag{3}$$

$$\mathbf{S} = \frac{1}{J} \begin{pmatrix} 0 \\ 0 \\ 0 \\ 0 \\ 0 \\ S_\nu \end{pmatrix} \tag{4}$$

where ρ is the density, p is the static pressure, and e is the total energy per unit mass. ν is kinematic viscosity and $\tilde{\nu}$ is the working variable related to eddy viscosity in S-A turbulence one equation model[13]. U, V and W are the contravariant velocities in ξ, η, ζ directions, and defined as

$$U = l_t + \mathbf{l} \bullet \mathbf{V} = l_t + l_x \tilde{u} + l_y \tilde{v} + l_z \tilde{w}$$
$$V = m_t + \mathbf{m} \bullet \mathbf{V} = m_t + m_x \tilde{u} + m_y \tilde{v} + m_z \tilde{w} \tag{5}$$
$$W = n_t + \mathbf{n} \bullet \mathbf{V} = n_t + n_x \tilde{u} + n_y \tilde{v} + n_z \tilde{w}$$

where J is the Jacobian of the coordinate transformation. l_t, m_t and n_t are the components of the interface contravariant velocity of the grid in ξ, η and ζ directions respectively. $\mathbf{l}$, $\mathbf{m}$ and $\mathbf{n}$ denote the normal vectors located at the centers of ξ, η and ζ interfaces of the control volume with their magnitudes equal to the surface areas and pointing to the directions of increasing ξ, η and ζ.

$$\mathbf{l} = \frac{\nabla \xi}{J}, \ \mathbf{m} = \frac{\nabla \eta}{J}, \ \mathbf{n} = \frac{\nabla \zeta}{J} \tag{6}$$

$$l_t = \frac{\xi_t}{J}, \ m_t = \frac{\eta_t}{J}, \ n_t = \frac{\zeta_t}{J} \tag{7}$$

In the generalized coordinates, $\Delta \xi = \Delta \eta = \Delta \zeta = 1$. The source term S_ν from the S-A model in Eq. (4), is given by

$$S_\nu = \bar{\rho} C_{b1} \left(1 - f_{t2} \right) \tilde{S} \tilde{\nu} + \frac{1}{Re} \left[-\bar{\rho} \left(C_{w1} f_w - \frac{C_{b1}}{\kappa^2} f_{t2} \right) \left(\frac{\tilde{\nu}}{d} \right)^2 \right.$$
$$\left. + \frac{\bar{\rho}}{\sigma} C_{b2} \left(\nabla \tilde{\nu} \right)^2 - \frac{1}{\sigma} \left(\nu + \tilde{\nu} \right) \nabla \tilde{\nu} \bullet \nabla \bar{\rho} \right] + Re \left[\bar{\rho} f_{t1} \left(\Delta q \right)^2 \right] \tag{8}$$

where

$$\chi = \frac{\tilde{\nu}}{\nu}, \quad f_{v1} = \frac{\chi^3}{\chi^3 + c_{v1}^3}, \quad f_{v2} = 1 - \frac{\chi}{1 + \chi f_{v1}}, \quad f_{t1} = C_{t1} g_t exp \left[-C_{t2} \frac{\omega_t^2}{\Delta U^2} \left(d^2 + g_t^2 d_t^2 \right) \right] \tag{9}$$

$$f_{t2} = C_{t3} exp \left(-C_{t4} \chi^2 \right), \quad f_w = g (\frac{1 + c_{w3}^6}{g^6 + c_{w3}^6})^{1/6}, \quad g = r + c_{w2}(r^6 - r) \tag{10}$$

5

$$g_t = min\left(0.1, \frac{\Delta q}{\omega_t \Delta x_t}\right), \quad \tilde{S} = S + \frac{\tilde{\nu}}{k^2 d^2 R_e} f_{v2}, \quad r = \frac{\tilde{\nu}}{\tilde{S} k^2 d^2 R_e} \tag{11}$$

where, ω_t is the wall vorticity at the wall boundary layer trip location, d is the distance to the closest wall, d_t is the distance of the field point to the trip location, Δq is the difference of the velocities between the field point and the trip location, Δx_t is the grid spacing along the wall at the trip location. The values of the coefficients are: $c_{b1} = 0.1355, c_{b2} = 0.622, \sigma = \frac{2}{3}, c_{w1} = \frac{c_{b1}}{k^2} + (1 + c_{b2})/\sigma, c_{w2} = 0.3, c_{w3} = 2, k = 0.41, c_{v1} = 7.1, c_{t1} = 1.0, c_{t2} = 2.0, c_{t3} = 1.1, c_{t4} = 2.0$.

The shear stress $\bar{\tau}_{ik}$ and total heat flux $\bar{q}_k$ in Cartesian coordinates is given by

$$\bar{\tau}_{ik} = (\mu + \mu_t) \left[\left(\frac{\partial \tilde{u}_i}{\partial x_k} + \frac{\partial \tilde{u}_k}{\partial x_i}\right) - \frac{2}{3}\delta_{ik}\frac{\partial \tilde{u}_j}{\partial x_j}\right] \tag{12}$$

$$\bar{q}_k = -\left(\frac{\mu}{Pr} + \frac{\mu_t}{Pr_t}\right)\frac{\partial \tilde{T}}{\partial x_k} \tag{13}$$

where μ is from Sutherland's law.

2.2 Time Marching Scheme

Following the dual time stepping method suggested by Jameson[14], an implicit pseudo time marching scheme using line Gauss-Seidel line relaxation is employed to solve the governing equations, as the following:

$$\frac{\partial \mathbf{Q}}{\partial t} = \frac{3\mathbf{Q^{n+1}} - 4\mathbf{Q^n} + \mathbf{Q^{n-1}}}{2\Delta t} \tag{14}$$

where $n-1$, n and $n+1$ are three sequential time levels, which have a time interval of Δt. The first-order Euler scheme is used to discretize the pseudo temporal term. The semi-discretized equations of the governing equations are given as the following:

$$\left[\left(\frac{1}{\Delta\hat{\tau}} + \frac{1.5}{\Delta t}\right)I - \left(\frac{\partial R}{\partial \mathbf{Q}}\right)^{n+1,m}\right]\delta\mathbf{Q^{n+1,m+1}} = R^{n+1,m} - \frac{3\mathbf{Q^{n+1,m}} - 4\mathbf{Q^n} + \mathbf{Q^{n-1}}}{2\Delta t} \tag{15}$$

where the $\Delta\hat{\tau}$ is the pseudo time step, and R stands for the net flux determined by the spatial high order numerical scheme, m is the iteration index for the pseudo time.

2.3 The Low Diffusion E-CUSP Scheme

The Low Diffusion E-CUSP(LDE) Scheme[15] is employed to calculate the inviscid fluxes. The key concept of LDE scheme is to split the inviscid flux into convective E^c and a pressure E^p based on characteristics analysis. In

generalized coordinate system, the flux $\mathbf{E}$ can be split as the following:

$$\mathbf{E}' = E^c + E^p = \begin{pmatrix} \rho U \\ \rho u U \\ \rho v U \\ \rho w U \\ \rho e U \\ \rho \tilde{\nu} U \end{pmatrix} + \begin{pmatrix} 0 \\ \xi_x p \\ \xi_y p \\ \xi_z p \\ p\overline{U} \\ 0 \end{pmatrix} \tag{16}$$

where, U is the contravariant velocity as defined in Eq. (5). $\overline{U}$ is defined as:

$$\overline{U} = U - \xi_t = \xi_x u + \xi_y v + \xi_z w \tag{17}$$

The convective flux, E^c is evaluated by

$$E^c = \rho U \begin{pmatrix} 1 \\ u \\ v \\ w \\ e \\ \tilde{\nu} \end{pmatrix} = \rho U f^c, \ f^c = \begin{pmatrix} 1 \\ u \\ v \\ w \\ e \\ \tilde{\nu} \end{pmatrix} \tag{18}$$

Let

$$C = c \left(\xi_x^2 + \xi_y^2 + \xi_z^2 \right)^{\frac{1}{2}} \tag{19}$$

where $c = \sqrt{\gamma R T}$ is the speed of sound. Then the convective flux at interface $i + \frac{1}{2}$ is evaluated as:

$$E^c_{i+\frac{1}{2}} = C_{\frac{1}{2}} \left[\rho_L C^+ f^c_L + \rho_R C^- f^c_R \right] \tag{20}$$

where, the subscripts L and R represent the left and right hand sides of the interface. The Mach number splitting of Edwards[16] is borrowed to determine C^+ and C^- as the following:

$$C_{\frac{1}{2}} = \frac{1}{2} \left(C_L + C_R \right) \tag{21}$$

$$C^+ = \alpha_L^+ \left(1 + \beta_L \right) M_L - \beta_L M_L^+ - M_{\frac{1}{2}}^+ \tag{22}$$

$$C^- = \alpha_R^- \left(1 + \beta_R \right) M_R - \beta_R M_R^- + M_{\frac{1}{2}}^- \tag{23}$$

$$M_L = \frac{U_L}{C_{\frac{1}{2}}}, \ M_R = \frac{U_R}{C_{\frac{1}{2}}} \tag{24}$$

$$\alpha_{L,R} = \frac{1}{2} \left[1 \pm sign \left(M_{L,R} \right) \right] \tag{25}$$

$$\beta_{L,R} = -max \left[0, 1 - int \left(|M_{L,R}| \right) \right] \tag{26}$$

$$M_{\frac{1}{2}}^+ = M_{\frac{1}{2}} \frac{C_R + C_L \Phi}{C_R + C_L} \tag{27}$$

$$M_{\frac{1}{2}}^- = M_{\frac{1}{2}} \frac{C_L + C_R \Phi^{-1}}{C_R + C_L} \tag{28}$$

7

$$\Phi = \frac{\left(\rho C^2\right)_R}{\left(\rho C^2\right)_L} \tag{29}$$

$$M_{\frac{1}{2}} = \beta_L \delta^+ M_L^- - \beta_R \delta^- M_R^+ \tag{30}$$

$$M_{L,R}^{\pm} = \pm \frac{1}{4} \left(M_{L,R} \pm 1\right)^2 \tag{31}$$

$$\delta^{\pm} = \frac{1}{2} \left\{ 1 \pm sign \left[\frac{1}{2} \left(M_L + M_R\right) \right] \right\} \tag{32}$$

The pressure flux, E^p is evaluated as the following

$$E^p_{i+\frac{1}{2}} = \begin{pmatrix} 0 \\ \mathcal{P}^+ p\, \xi_x \\ \mathcal{P}^+ p\, \xi_y \\ \mathcal{P}^+ p\, \xi_z \\ \frac{1}{2} p \left[\overline{U} + \overline{C}_{\frac{1}{2}} \right] \\ 0 \end{pmatrix}_L + \begin{pmatrix} 0 \\ \mathcal{P}^- p\, \xi_x \\ \mathcal{P}^- p\, \xi_y \\ \mathcal{P}^- p\, \xi_z \\ \frac{1}{2} p \left[\overline{U} - \overline{C}_{\frac{1}{2}} \right] \\ 0 \end{pmatrix}_R \tag{33}$$

The contravariant speed of sound $\overline{C}$ in the pressure vector is consistent with $\overline{U}$. It is computed based on C as the following,

$$\overline{C} = C - \xi_t \tag{34}$$

The use of $\overline{U}$ and $\overline{C}$ instead of U and C in the pressure vector is to take into account of the grid speed so that the flux will transit from subsonic to supersonic smoothly. When the grid is stationary, $\xi_t = 0$, $\overline{C} = C$, $\overline{U} = U$. The pressure splitting coefficient is:

$$\mathcal{P}_{L,R}^{\pm} = \frac{1}{4} \left(M_{L,R} \pm 1\right)^2 \left(2 \mp M_L\right) \tag{35}$$

The LDE scheme can capture crisp shock profile and exact contact surface discontinuities as accurately as the Roe scheme[15].

2.4 The 5th Order WENO Scheme

For reconstruction of the interface flux, $E_{i+\frac{1}{2}} = E(Q_L, Q_R)$, the conservative variables Q_L and Q_R are evaluated by using the 5th order WENO scheme[17, 18]. For example,

$$(Q_L)_{i+\frac{1}{2}} = \omega_0 q_0 + \omega_1 q_1 + \omega_2 q_2 \tag{36}$$

where

$$q_0 = \frac{1}{3} Q_{i-2} - \frac{7}{6} Q_{i-1} + \frac{11}{6} Q_i \tag{37}$$

$$q_1 = -\frac{1}{6} Q_{i-1} + \frac{5}{6} Q_i + \frac{1}{3} Q_{i+1} \tag{38}$$

$$q_2 = \frac{1}{3} Q_i + \frac{5}{6} Q_{i+1} - \frac{1}{6} Q_{i+2} \tag{39}$$

$$\omega_k = \frac{\alpha_k}{\alpha_0 + \ldots + \alpha_{r-1}} \tag{40}$$

8

$$\alpha_k = \frac{C_k}{\epsilon + IS_k}, \; k = 0, \ldots, r - 1 \tag{41}$$

$$C_0 = 0.1, \; C_1 = 0.6, \; C_2 = 0.3 \tag{42}$$

$$IS_0 = \frac{13}{12} \left(Q_{i-2} - 2Q_{i-1} + Q_i \right)^2 + \frac{1}{4} \left(Q_{i-2} - 4Q_{i-1} + 3Q_i \right)^2 \tag{43}$$

$$IS_1 = \frac{13}{12} \left(Q_{i-1} - 2Q_i + Q_{i+1} \right)^2 + \frac{1}{4} \left(Q_{i-1} - Q_{i+1} \right)^2 \tag{44}$$

$$IS_2 = \frac{13}{12} \left(Q_i - 2Q_{i+1} + Q_{i+2} \right)^2 + \frac{1}{4} \left(3Q_i - 4Q_{i+1} + Q_{i+2} \right)^2 \tag{45}$$

ϵ is originally introduced to avoid the denominator becoming zero and is supposed to be a very small number. In [18], it is observed that IS_k will oscillate if ϵ is too small and also shift the weights away from the optimal values in the smooth region. The higher the ϵ values, the closer the weights approach the optimal values, C_k, which will give the symmetric evaluation of the interface flux with minimum numerical dissipation. When there are shocks in the flow field, ϵ can not be too large to maintain the sensitivity to shocks. In [18], $\epsilon = 10^{-2}$ is recommended for the transonic flow with shock waves. In the current work since there is no shock in the flow, the $\epsilon = 0.3$ is used.

The viscous terms are discretized by a fully conservative fourth-order accurate finite central differencing scheme suggested by Shen et al. [19, 20].

2.5 Boundary Conditions

Steady state freestream conditions including total pressure, total temperature, and two flow angles are specified for the upstream portion of the far field boundary. For far field downstream boundary, the static pressure is specified as freestream value to match the intended freestream Mach number. The streamwise gradients of other variables are forced to vanish. The periodic boundary condition is used in the spanwise direction. The wall treatment suggested in [18] to achieve flux conservation by shifting half interval of the mesh on the wall is employed. If the wall surface normal direction is in η-direction, the no-slip condition is enforced on the surface by computing the wall inviscid flux $F_{1/2}$ in the following manner:

$$\mathbf{F_w} = \begin{pmatrix} \rho V \\ \rho u V + p\eta_x \\ \rho v V + p\eta_y \\ \rho w V + p\eta_z \\ (\rho e + p)V \end{pmatrix}_w = \begin{pmatrix} 0 \\ p\eta_x \\ p\eta_y \\ p\eta_z \\ 0 \end{pmatrix}_w \tag{46}$$

Total pressure, total temperature are specified as the inlet boundary conditions in the injection cavity. Constant static pressure is used in the suction cavity.

2.6 Mesh

The 3D structured meshes are constructed using the O-mesh topology in order to achieve high mesh quality within the airfoil boundary. A total of 601 points are placed around the airfoil, 301 points on the upper surface, 301 points on the pressure surface and 121 points normal to the airfoil with an additional 41 points across the jet. The mesh consists of 10,112,000 cells and is partitioned into 216 blocks for parallel computation. The far-field
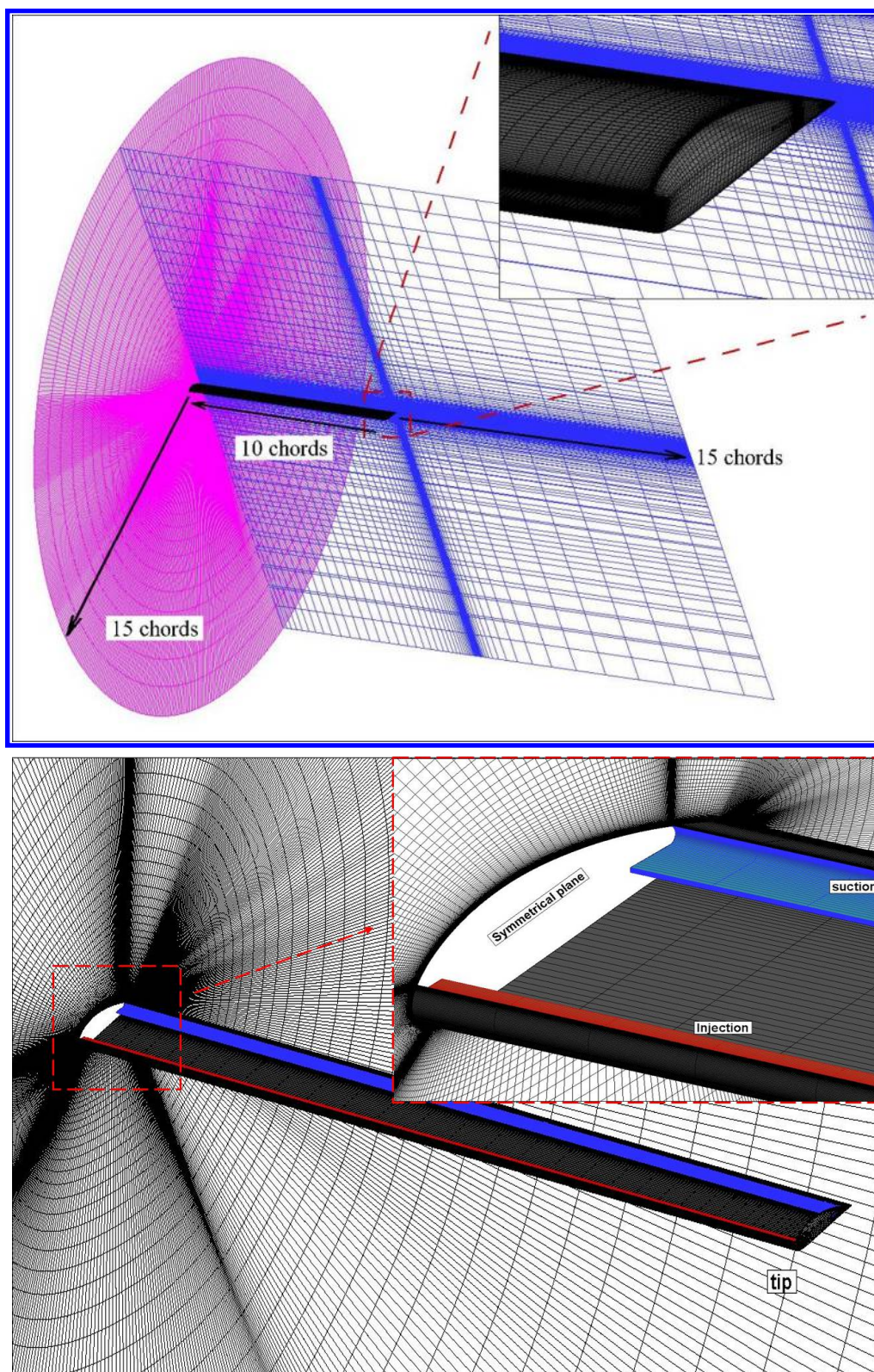
Figure 4: Computational mesh for CFJ calculation (AoA = 5°)

boundary is located 15 chords away from the airfoil. To resolve the turbulent boundary layer, the first grid point is placed at $y^+ \approx 1$. The block definition is found in 1 and the mesh topology is shown in Fig. 4.

Table 1: Mesh details for CFJ 6421

Block	ξ-Direction	η-Direction	ζ-Direction	Cell number	location
1-180	60	20	40	48000	around the airfoil
181-192	50	24	40	48000	Wing Tip blocks
193-200	20	40	40	32000	Injection blocks
201-208	30	40	40	48000	Connection blocks
209-216	20	40	40	32000	Suction blocks
Total mesh size				10,112,000	

3   CFJ Parameters

This section defines the important parameters to evaluate a CFJ airfoil performance.

3.1   Lift and Drag Calculation

The momentum and pressure at the injection and suction slots produce a reactionary force, which is automatically measured by the force balance in wind tunnel testing. However, for CFD simulation, the full reactionary force needs to be included. Using control volume analysis, the reactionary force can be calculated using the flow parameters at the injection and suction slot opening surfaces. Zha et al. [2] give the following formulations to calculate the lift and drag due to the jet reactionary force for a CFD simulation. By considering the effects of injection and suction jets on the CFJ airfoil, the expressions for these reactionary forces are given as :

$$F_{x_{cfj}} = (\dot{m}_j V_{j1} + p_{j1} A_{j1}) * \cos(\theta_1 - \alpha) - (\dot{m}_j V_{j2} + p_{j2} A_{j2}) * \cos(\theta_2 + \alpha) \tag{47}$$

$$F_{y_{cfj}} = (\dot{m}_{j1} V_{j1} + p_{j1} A_{j1}) * \sin(\theta_1 - \alpha) + (\dot{m}_{j2} V_{j2} + p_{j2} A_{j2}) * \sin(\theta_2 + \alpha) \tag{48}$$

where the subscripts 1 and 2 stand for the injection and suction respectively, and θ_1 and θ_2 are the angles between the injection and suction slot surfaces and a line normal to the airfoil chord. α is the angle of attack.

The total lift and drag on the airfoil can then be expressed as:

$$D = R'_x - F_{x_{cfj}} \tag{49}$$

$$L = R'_y - F_{y_{cfj}} \tag{50}$$

where R'_x and R'_y are the surface integral of pressure and shear stress in x (drag) and y (lift) direction excluding the internal ducts of injection and suction. For the CFD simulation, the total lift and drag are calculated using Eqs. (49) and (50).

3.2   Jet Momentum Coefficient C_μ

The jet momentum coefficient C_μ is a parameter used to quantify the injection intensity. It is defined as :

$$C_\mu = \frac{\dot{m}V_j}{\frac{1}{2}\rho_\infty V_\infty^2 S} \tag{51}$$

where $\dot{m}$ is the injection mass flow, V_j the injection velocity, ρ_∞ and V_∞ denote the free stream density and velocity, and S is the platform area.

3.2.1 C_μ Iteration:

To achieve zero net mass flux with the CFJ flow control, the mass flow exiting the injection slot must be equal to the mass flow entering the suction slot, i.e. $\dot{m}_{inj} = \dot{m}_{suc}$. The prescribed jet momentum coefficient C_μ is achieved by adjusting the injection cavity total pressure. Total temperature is assumed constant during this process. The injection and suction mass flow rates are matched by adjusting the suction cavity static pressure. The iterative process is conducted throughout the simulation until the specified momentum coefficient is reached and the injection and suction mass flow match within the acceptable tolerance, which is 0.2% for the present study.

3.3   Power Coefficient P_c

The CFJ can be implemented by mounting a pumping system inside the wing that withdraws air from the suction slot and blows it into the injection slot. The power consumption can be determined by the jet mass flow and total enthalpy change as the following :

$$P = \dot{m}(H_{t1} - H_{t2}) \tag{52}$$

where H_{t1} and H_{t2} are the total enthalpy in the injection cavity and suction cavity respectively, P is the Power required by the pump and $\dot{m}$ the jet mass flow rate. Introducing the pumping efficiency η and total pressure ratio of the pump $\Gamma = \frac{P_{t1}}{P_{t2}}$, the power consumption can be expressed as :

$$P = \frac{\dot{m}C_p T_{t2}}{\eta}(\Gamma^{\frac{\gamma-1}{\gamma}} - 1) \tag{53}$$

The power consumption can be expressed as a power coefficient below:

$$P_c = \frac{P}{\frac{1}{2}\rho_\infty V_\infty^3 S} \tag{54}$$

In this research, the pumping efficiency of 100% is used for all the simulations unless indicated otherwise.

3.4   Corrected Aerodynamic Efficiency

The conventional airfoil aerodynamic efficiency is defined as $\frac{L}{D}$. However since CFJ active flow control consumes energy, the CFJ corrected aerodynamic efficiency is modified to take into account the energy consumption of the pump. The formulation of the corrected aerodynamic efficiency for CFJ airfoils is :

$$(\frac{L}{D})_c = \frac{L}{D + \frac{P}{V_\infty}} = \frac{C_L}{C_D + P_c} \tag{55}$$

12

where V_∞ is the free stream velocity, P is the CFJ pumping power, and L and D are the lift and drag generated by the CFJ airfoil. This formulation converts the power consumed by the CFJ into the drag of the airfoil. If the pumping power is set to 0, this formulation returns to the aerodynamic efficiency of a conventional airfoil.

3.5 Aircraft Productivity

To compare aircraft that have the same ratio of initial weight to final weight with the same engine fuel consumption or battery energy density, the productivity efficiency C_L^2/C_D is introduced to measure the productivity parameter [1].

The productivity efficiency $C_L^2/C_D = C_L(C_L/C_D)$ is a more comprehensive parameter than the conventional aerodynamic efficiency C_L/C_D to measure the merit of an airplane aerodynamic design for cruise performance. The former includes not only the information of C_L/C_D, but also the information of the aircraft weight C_L. For example, for two airplane designs having the same C_L/C_D with one C_L twice larger than the other, if the wing sizes are the same, one airplane will be able to carry twice more weight than the other with productivity and wing loading increased by 100%. Such a large difference is not reflected by C_L/C_D, but very well reflected by C_L^2/C_D.

The definition of C_L/C_D in general is a suitable measure of merit for conventional aircraft design. This is because at a certain Mach number regime, the maximum C_L/C_D is usually achieved at the low angle of attack within the drag bucket and is more or less the same for different airfoil designs. In other words, for the same optimum C_L/C_D, the C_L is about the same. A typical C_L for a subsonic airfoil is about 0.4 and for a transonic airfoil is about 0.7.

For CFJ airfoil, the minimum CFJ pumping power occurs at a fairly high AoA [8, 10]. With the augmentation of CFJ, the subsonic cruise lift coefficient of a CFJ airfoil is typically 2 to 3 times higher than the conventional airfoil with about the same $(C_L/C_D)_c$ [21]. Such a high lift coefficient is unattainable for conventional airfoil since they would be either stalled or near stalled with very high drag. Hence for CFJ aircraft design, the productivity efficiency $C_L^2/C_D = C_L(C_L/C_D)$ is more informative to be used to reflect the aerodynamic performance. The corrected productivity efficiency for CFJ airfoils is $(C_L^2/C_D)_c = C_L^2/(C_D + P_c)$.

4 Results and Discussion

Table 2: Computational parameters 3D CFJ wing

cases	Mach	Reynolds	AoA	C_μ
CFJ wing,AR=20	0.063	3,030,000	25°, 45°, 70°	0.15, 0.2, 0.25, 0.3

For the low speed takeoff/landing CFJ wing simulation, the Mach number of 0.063 and Reynolds number of 3.03 million are used. The jet momentum coefficients $C\mu = 0.15, 0.2, 0.25$, and 0.3 are simulated at different AoAs of 25°, 45° and 70°. The results of the CFJ wing with aspect ratio of 20 is presented first. The 3D effect due to reduced aspect ratio to 10 and 5 are compared after. Table 2 summarizes the simulation parameters for the case of AR=20.

A mesh refinement study was performed for the CFJ6421 wing by adjusting the mesh size in the chord-wise and wall-normal direction, as shown in Table 3 and **??**. The baseline mesh size of $601 \times 151 \times 81$ is placed on the CFJ wing surface. The C_L, C_D results are converged based on mesh size as shown in Table 3.

Table 3: Mesh independence study for the CFJ6421 wing at AoA=45° and C_μ=0.15.

Case	AoA	Grid size	C_L	C_D
1	45	$301 \times 121 \times 81$	6.18	1.54
2	45	$601 \times 61 \times 81$	4.88	0.47
3	45	$601 \times 121 \times 81$	4.92	0.46
4	45	$1201 \times 121 \times 81$	4.87	0.458

Table 4: Lift and drag coefficients at different angle of attacks

AoA	C_μ	C_L	C_D	P_c	L/D	C_L/C_{Dc}	C_L^2/C_D	C_L^2/C_{Dc}
	0.15	3.392	0.173	0.972	19.6	2.96	66.50	10.048
25	0.2	3.566	0.113	1.856	31.55	1.75	112.534	6.458
	0.25	3.74	0.144	2.6762	25.97	1.326	97.14	4.96
45	0.15	4.94	0.46	0.938	10.74	3.53	53.05	17.45
	0.25	5.54	0.497	2.695	11.14	1.735	61.75	9.615
70	0.25	7.26	1.05	2.818	6.91	1.88	50.20	13.65
	0.30	7.81	1.183	4.374	6.6	1.405	51.56	10.976

4.1 Lift and Drag Coefficient of CFJ Wing, AR=20

Table 4 shows the computed lift and drag coefficients at different AoAs and different jet momentum coefficients. For all the simulated cases, the lift coefficients for CFJ wings are substantially higher than the conventional wings. The lift coefficients of 7.26 is obtained at AoA of 70° and $C_\mu = 0.25$. Note that for the 2D airfoil study at this condition, the lift coefficient of 8.3 is achieved. The lift coefficient along the wing span is attenuated toward the wing-tip due to the tip vortex of finite-span wing. Moreover, the drag coefficient is increased to $C_D = 1.05$ compared to the C_D=0.314 in the 2D airfoil simulation.

If we compare the aerodynamic efficiency parameter L/D, the maximum aerodynamic efficiency of 31.55 is achieved at the AoA = 25 and $C_\mu = 0.25$. The obtained aerodynamic efficiency is substantially enhanced than conventional wing at Takeoff/Landing. As the angle of attack gets higher, the aerodynamic efficiency L/D decreases, since the drag coefficient increases faster than lift coefficient. The more comprehensive efficiency parameter to evaluate the energy expenditure of the whole wing is the corrected aerodynamics efficiency C_L/C_{D_c}. For the investigated simulations, the best C_L/C_{D_c} is obtained at AoA = 45 and $C_\mu = 0.15$. And the best corrected productivity efficiency parameter C_L^2/C_{D_c} of 17.45 is also achieved at the same condition.

Table 4 also gives the power efficiency parameters considering the Co-Flow Jet pumping power. For takeoff and landing, the aerodynamic efficiency is reduced because of higher drag. The maximum pure aerodynamic efficiency L/D of 31.55 is observed at AoA = 25° and C_μ=0.2. Considering the CFJ pumping power, the best corrected aerodynamic efficiency C_L/C_{Dc} of 10.739 is obtained at AoA = 45° and $C_\mu = 0.15$, where the maximum corrected productivity efficiency C_L^2/C_{Dc} of 17.45 is obtained. The reason of the higher efficiency at this condition is that the lift is relatively high and the power consumption is fairly low. Therefore, the best efficiency point is at AoA=45° and $C_\mu = 0.15$.

Fig. 5 shows the comparison of the lift and drag coefficients for 3D wing and 2D airfoil simulation at different
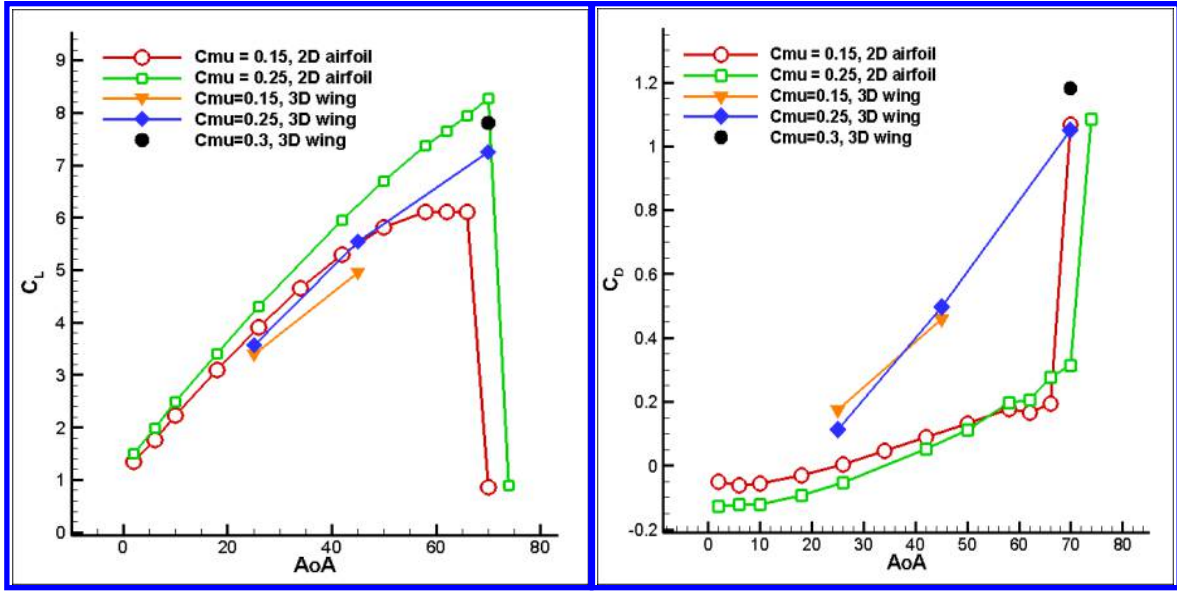
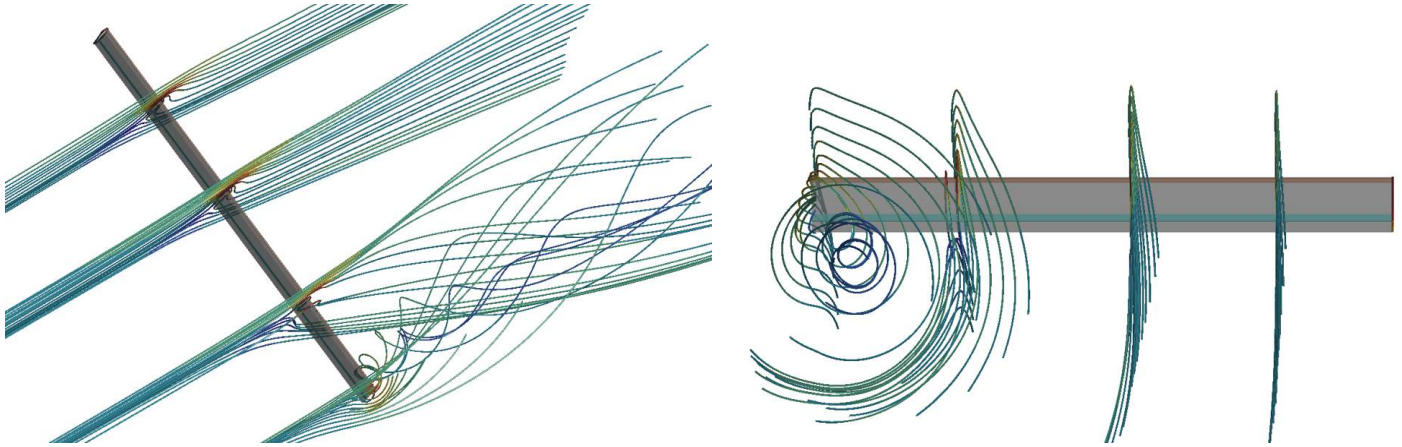Figure 5: Lift and drag coefficient of 3D CFJ wing and 2D airfoil

Figure 6: Three-dimensional streamlines on CFJ wing with finite span

$C_\mu = 0.15$ and 0.25. The lift coefficient of the 3D wing with AR of 20 is decreased by 12% compared to the 2D airfoil. The drag coefficient of 3D wing is increased by 234%-244% compared to the 2D airfoil at the jet momentum condition of $C_\mu = 0.25$. As shown in Table 4 and Fig. 5, the lift coefficient reaches 7.81 at C_μ of 0.3 and AoA of $70°$. This coefficient is greater than 7.6, which is the theoretical limit of the 2D airfoil used to form the 3D wing.

4.2   High Lift CFJ Wing Flow Structures, AR=20

Figs. 7, 8 and 9 show the Mach number contours at different spans across the wing at the AoA of $25°, 45°, 70°$ for the wing with AR of 20. The flow is accelerated near the leading edge and is very well attached, which is induced by the high momentum jet across the whole wing except for the wing tip region. Comparing the Mach number contours on the suction surface for three AoAs, the higher the AoAs and C_μs, the high higher the peak Mach number near leading edge. It means that the main flow is strongly induced by the mixing effect of the very high-velocity jet. Moreover, considering the wing tip, there exists a region of flow separation induced by the tip

15
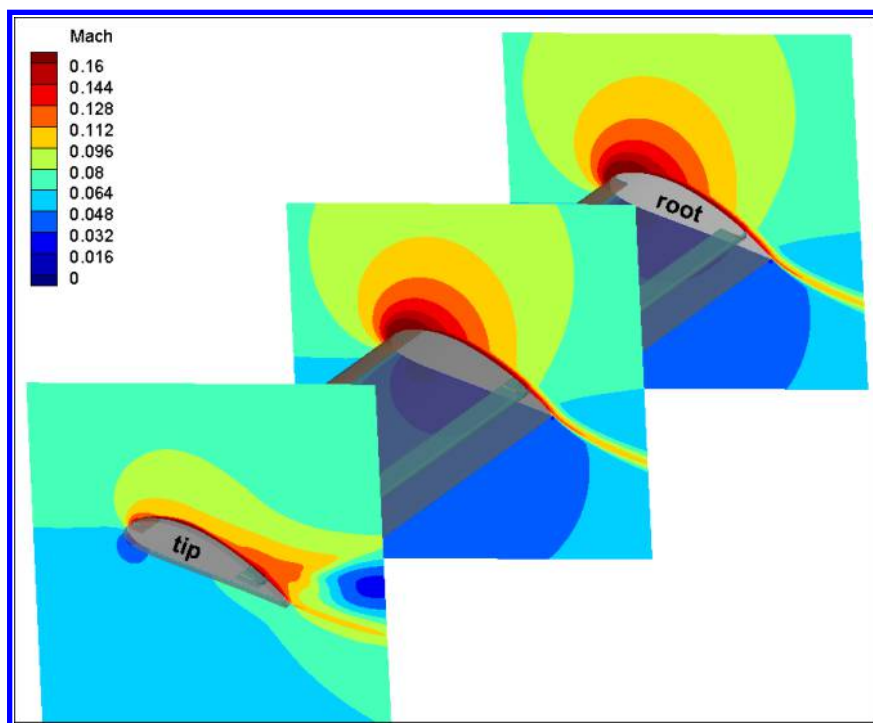
Figure 7: Mach number contours at AoA=25° and C_μ=0.2
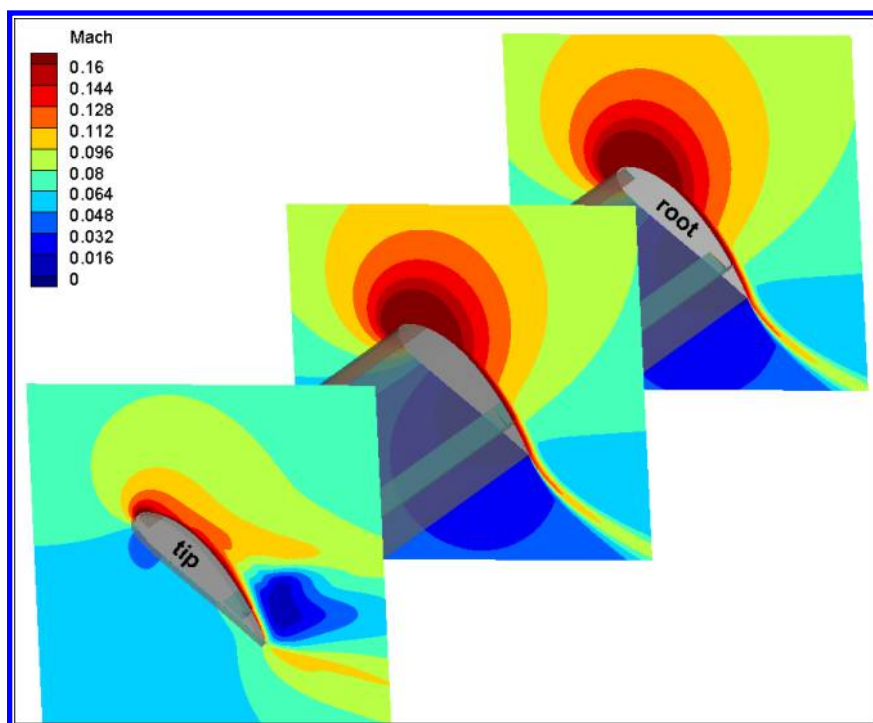
Figure 8: Mach number contours at AoA=45° and C_μ=0.25

16
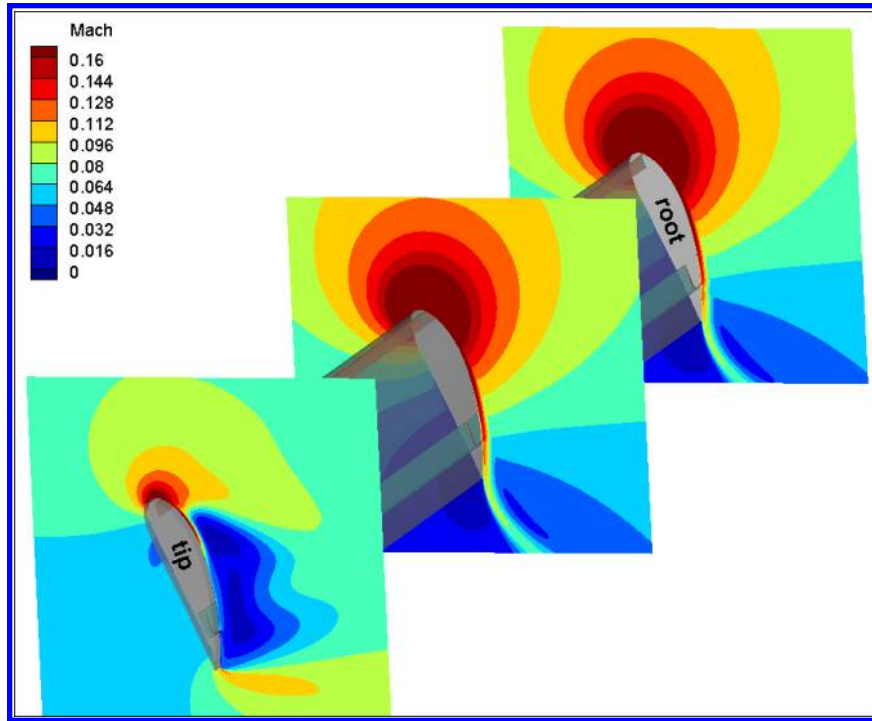
Figure 9: Mach number contours at AoA=70°

vortex. As the AoA increases, the separation region tends to become larger. Because of the roll-up of wingtip vortex, the rotating wingtip flow interacts with the high-speed jet flow, created the strong interaction and large separation at the wingtip region. The wingtip separated flow could explain the high drag coefficient at high AoA of 70°.

4.3 High Lift CFJ Wing Pressure Distribution, AR=20

Figs.10, 11 and 12 shows the pressure contours at different spans across the wing at different AoAs. The pressure on the upper surface of the CFJ wing is substantially lower than conventional wing. The lower pressure region is created by the strong flow acceleration induced by the Co-Flow Jet. The lowest pressure region is observed at near the leading edge, which corresponds to the super-suction effect of the leading edge.

At the wingtip region, the flow is formed by the high-speed co-flow jet and the rolling-up wingtip vortex. The rolling-up flow at the wingtip is enhanced by the very large pressure difference. The air flow rolls up from the lower surface to the upper surface and created the flow separation on the upper surface, thus generating a low-pressure region near the trailing edge. As the AoA gets higher, the separation point becomes closer to the leading edge, and the separation region grows larger. This large low-pressure region on the upper surface accounts for the large drag at high AoA.

To better visualize the flow field, the pressure contours with streamlines at AoA = 45° are plotted in Fig. 13. For the streamlines near the tip, due to the extremely high-pressure difference between the upper surface and lower surface, the strong tip vortex is generated in a way that the secondary flow is migrated from the lower surface to the upper surface through the wing-tip region. The tip vortex is thus generated, which will affect the flow structures on the upper surface and reduce the lift.
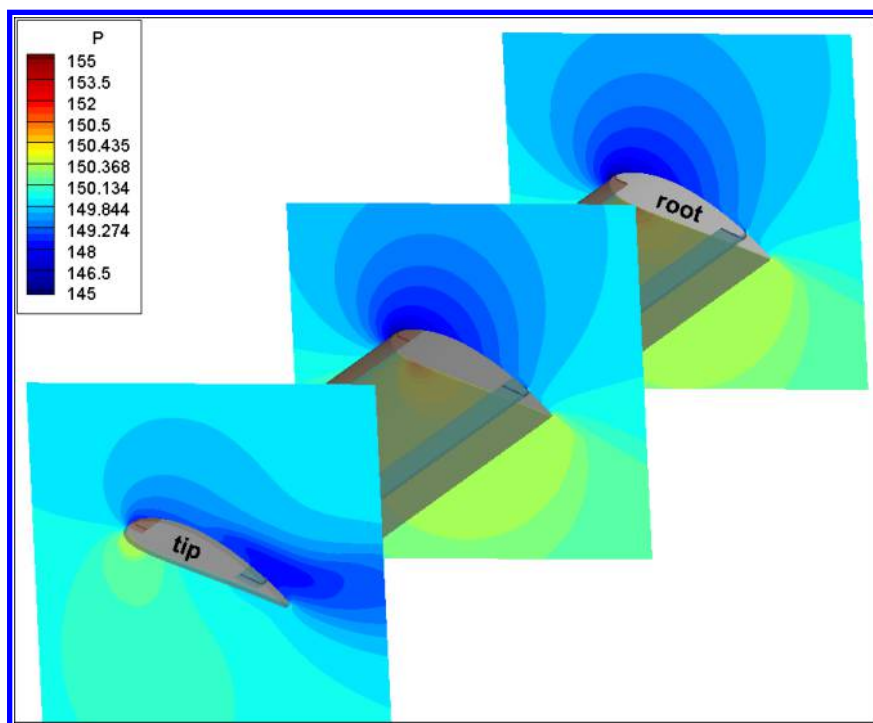
17

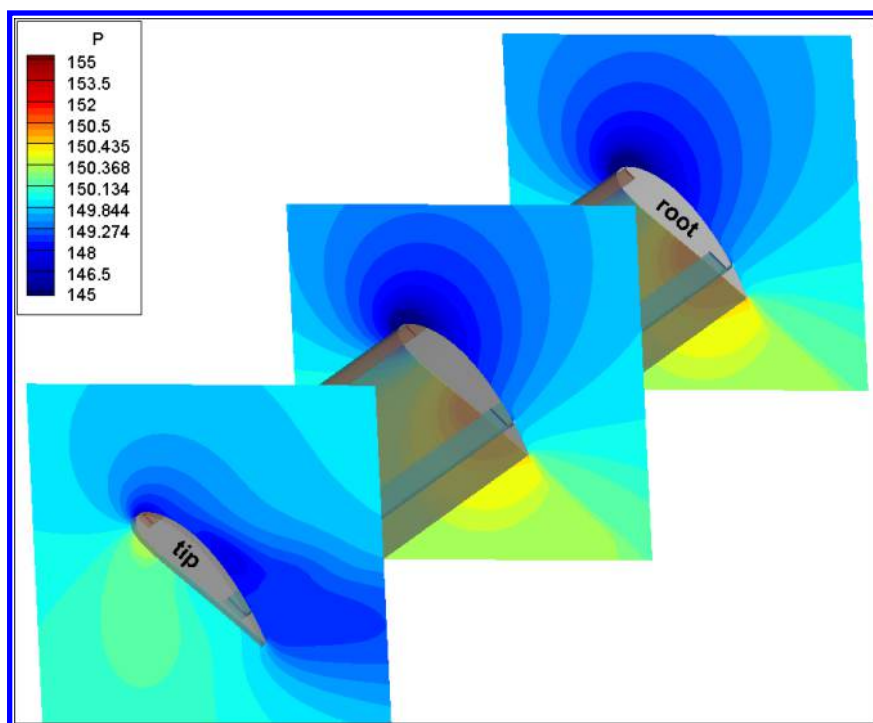Figure 10: Pressure contours of different spanwise crosssection at AoA=25° and C_μ=0.2

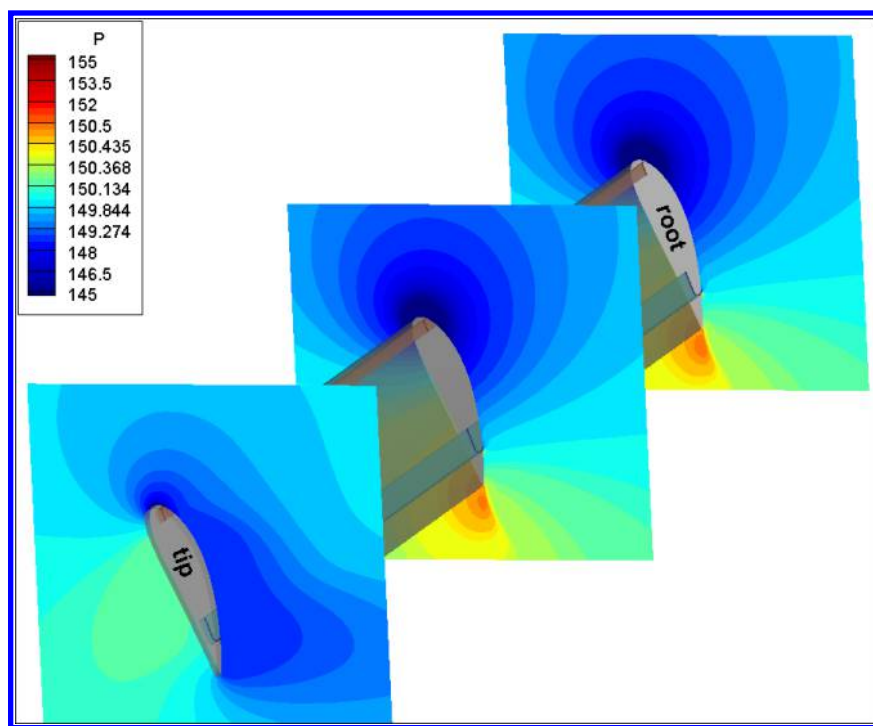Figure 11: Pressure contours of different spanwise crosssection at AoA=45° and C_μ=0.25

Figure 12: Pressure contours of different spanwise crosssection at AoA=70° and C_μ=0.25
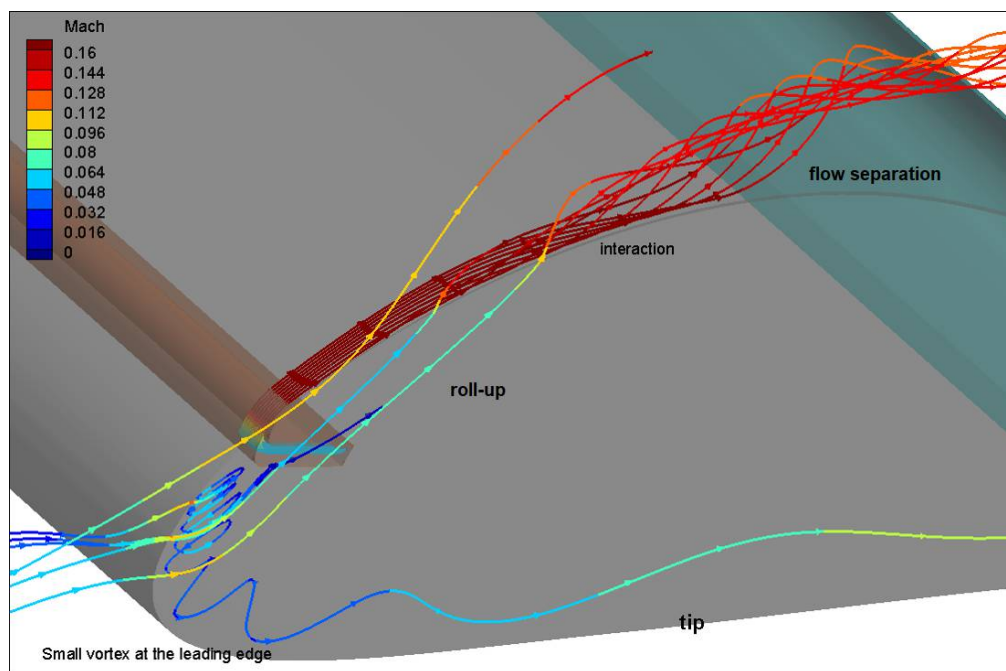

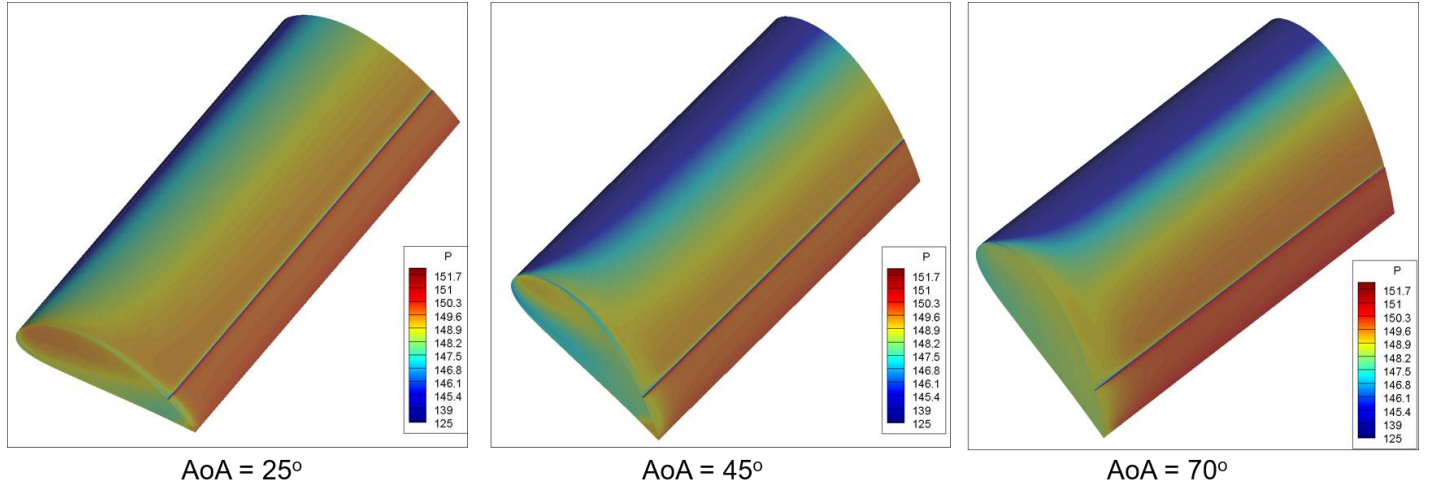Figure 13: streamlines near the wing tip showing the interaction of CFJ and tip vortex

Figure 14: Pressure distribution on the wing surface at 3 angles of attack.
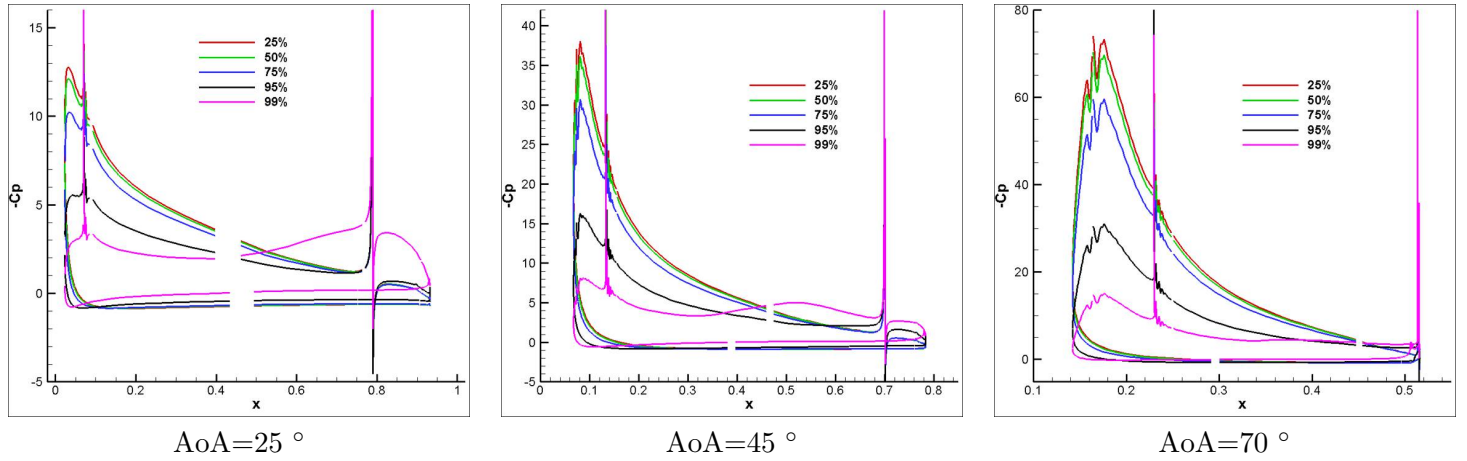

Figure 15: Pressure coefficient C_p at different span at the AoA of 25 °, 45 °, and 70 °.

The pressure contours on the wing surfaces are shown in Fig. 14. For all the CFJ wing simulation, the pressure at the leading edge is very low due to the super-suction effect induced by the CFJ. It contributes to the high lift generated by CFJ wing.

The local lift loading can be seen from the pressure coefficient (C_p) and isentropic Mach number plots M_{is} shown in Figs. 15 and 16. The spikes at 3% and 80% chord correspond to the injection and suction slot location respectively, where the wing upper surface is discontinuous.

All C_p plots show that the peak pressure coefficient $C_{p_{max}}$ obtained is much higher than the traditional airfoil. For AoA of 70°, the maximum pressure coefficient $C_{p_{max}}$ at the leading edge is greater than 70 with the peak Mach number of 0.65, 10 times higher than the freestream Mach number. The high suction peak near the LE, which contributes to the lift increase and the pressure drag decrease. Also, all C_p plots show that the lift loading is fairly uniform in the inner 75% wingspan, while the outer 25% span loading near the wingtip is reduced by the strong wingtip vortex.

To investigate whether the lowest pressure region is located at the leading edge of the wing or inside the tip
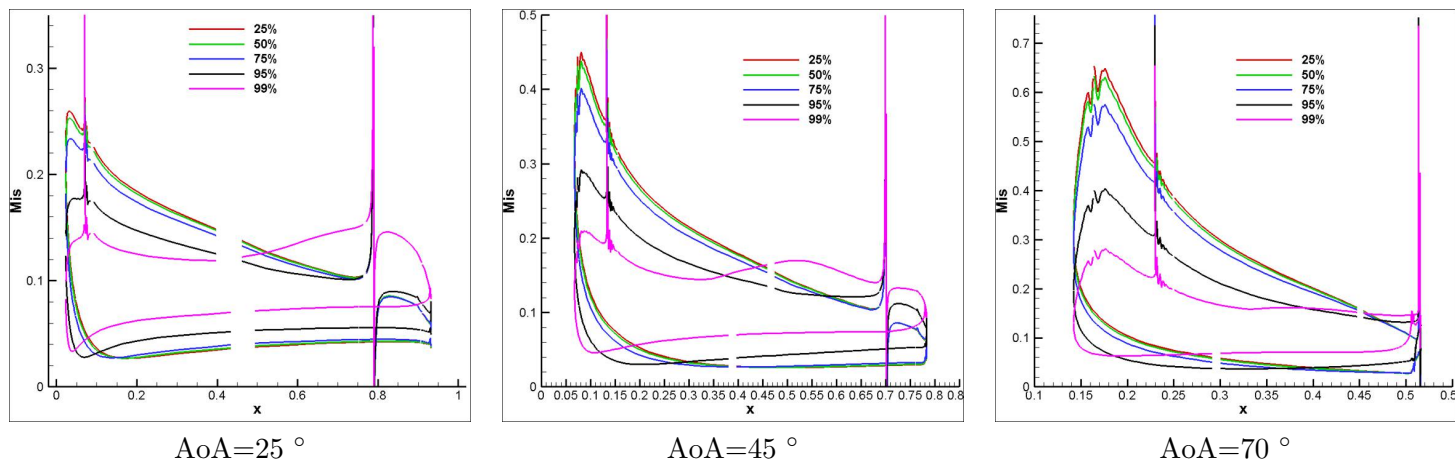
20

AoA=25 °　　　　　　　　　　AoA=45 °　　　　　　　　　　AoA=70 °

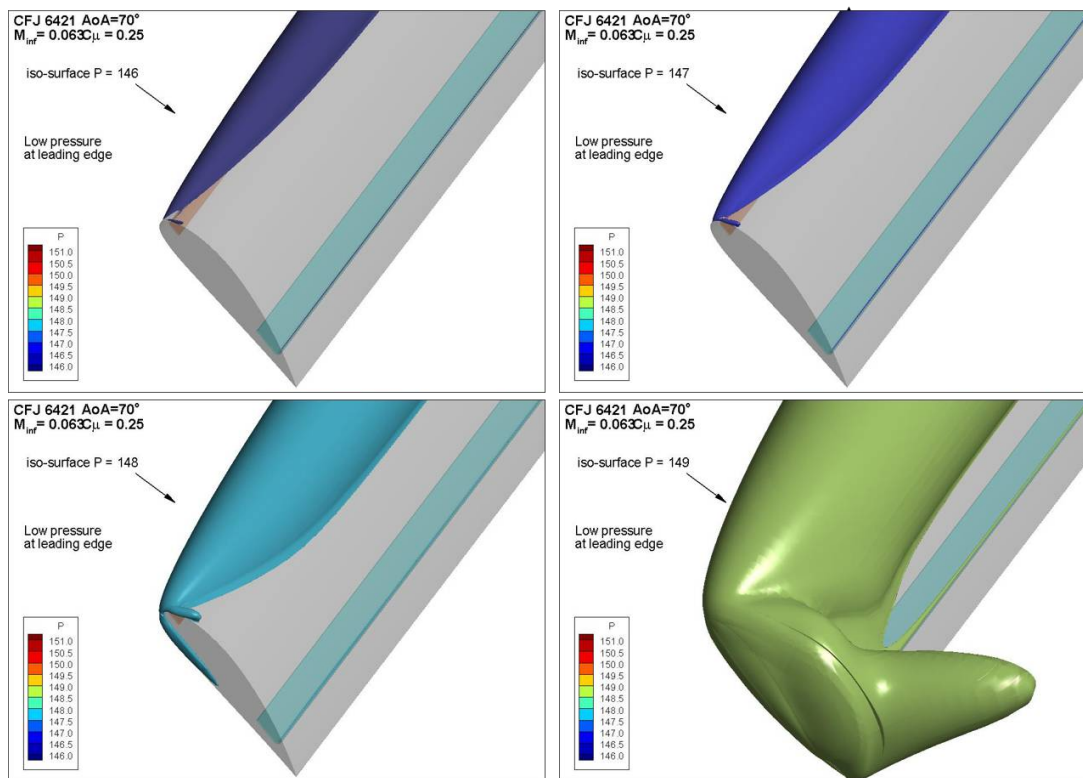Figure 16: Isentropic Mach number M_{is} at different span at the AoA of 25 °, 45 °, and 70 °

Figure 17: Iso-pressure surfaces at the wing-tip

21

Table 5: The zero-lift drag coefficient C_{D0} at different C_μ.

C_μ	AoA	C_{D0}
0.15	-9.5°	-0.056
0.25	-10.5°	-0.106

vortex core, the normalized iso-pressure surfaces with the values of 146, 147, 148, and 149 are plotted in Fig. 17 at the AoA of 70° near the tip region. Fig. 17 indicates that the lowest pressure is obtained at the wing leading edge.

4.4 Oswald Efficiency of the CFJ Wing

To investigate the induced drag effect due to the ultra-lift coefficient of the CFJ wing, the Oswald efficiency of the wing is studied with the aspect ratio of 20, 10 and 5. The Oswald efficiency represents the induced drag increase due to lift of a three-dimensional wing, as compared with an ideal wing having the same aspect ratio and an elliptical lift distribution. The Oswald efficiency e_0 is defined by the drag polar equation:

$$C_D = C_{D0} + \frac{C_L^2}{\pi e_0 AR} \tag{56}$$

where C_D is the total drag coefficient, C_{D0} is the zero lift drag coefficient of the wing. The induced drag coefficient is

$$C_{Di} = \frac{C_L^2}{\pi e_0 AR} \tag{57}$$

For conventional fixed-wing with moderate aspect ratio and sweep, Oswald efficiency is typically between 0.7 and 0.85.

The zero-lift drag coefficient C_{D0} varies with the jet momentum coefficient C_μ. In this paper, C_{D0} is calcualted by 2D RANS simulation at zero lift with the same C_μ of the 3d CFJ wing. A 2D airfoil naturally does not have induced drag. A comparison conducted in our group for the zero lift drag coefficient between 2D airfoil and 3D wing indicates that the difference is small. Table 5 gives the values of C_{D0} and its AoA at different C_μ.

Following the equation (56), the Oswald efficiency e_0 are calculated for different aspect ratio and C_μ as shown in Table 6. Interestingly, the Oswald efficiency is increased with the AR decreased from 20 to 5 at the same AoA and C_μ. It achieves the value as high as 0.967 for AR of 5, C_μ of 0.25 and AoA of 25°. This value is substantially higher than the Oswald efficiency of conventional wing with no flow control. If it is proved to be true, it means that the penalty of induced drag for 3D CFJ wing is smaller than the conventional wing even though the total induced drag coefficient is still increased with decreasing AR. The lowest value of the Oswald efficiency is 0.726 occurring at aspect ratio =20 with $C_\mu = 0.25$ and AoA =70°.

5   Conclusion

This paper conducts three-dimensional RANS simulation of Co-Flow Jet wings with different aspect ratios at higher angle of attack and jet momentum C_μ in order to investigate the ultra-high lift performance. The 3D RANS CFD solver employs the Spalart-Allmaras (S-A) one-equation turbulence model, 5th order WENO scheme for the inviscid fluxes, and 4th order central differencing for the viscous terms. The study indicates that CFJ

Table 6: Oswald efficiency e_0 calcualted for the finite CFJ wing

C_μ	AR	AoA	C_L	C_D	zero-lift drag coefficient C_{D0}	Oswald efficiency e_0
0.15	5	25	2.518	0.393	-0.056	0.899
0.15	5	45	3.642	0.92	-0.056	0.865
0.15	10	25	3.03	0.286	-0.056	0.854
0.15	10	45	4.42	0.719	-0.056	0.802
0.15	20	25	3.392	0.173	-0.056	0.800
0.15	20	45	4.94	0.46	-0.056	0.753
0.25	5	25	2.747	0.391	-0.106	0.967
0.25	5	45	3.96	1.07	-0.106	0.849
0.25	10	25	3.322	0.272	-0.106	0.929
0.25	10	45	4.85	0.786	-0.106	0.839
0.25	20	25	3.74	0.144	-0.106	0.890
0.25	20	45	5.54	0.497	-0.106	0.810
0.25	20	70	7.26	1.05	-0.106	0.726

active flow control wing is able to achieve the maximum lift coefficient of 7.8 without flaps at a very high AoA of 70° with fairly good aerodynamic efficiency for the take-off/landing flow conditions. For high AoAs, the outer 25% wingspan is affected most by the wingtip vortex contributing the lift reduction and drag increase. The Oswald efficiency is increased with the AR decreased from 20 to 5 at the same AoA and C_μ. It achieves the value as high as 0.967 for AR of 5, C_μ of 0.25 and AoA of 25°, indicating that the penalty of induced drag for 3D CFJ wing is small with decreased aspect ratio even though very high lift coefficient is obtained. The lowest value of the Oswald efficiency is 0.726 occurring at AR of 20, C_μ of 0.25, and AoA of 70°.

6 Acknowledgment

References

[1] Yunchao Yang and Gecheng Zha, "Super-Lift Coefficient of Active Flow Control Airfoil: What is the Limit?." AIAA Paper 2017-1693, AIAA SCITECH2017, 55th AIAA Aerospace Science Meeting, Grapevine, January 9-13 2017.

[2] G.-C. Zha, W. Gao, and C. Paxton, "Jet Effects on Co-Flow Jet Airfoil Performance," *AIAA Journal, No. 6,*, vol. 45, pp. 1222–1231, 2007.

[3] G.-C. Zha and D. C. Paxton, "A Novel Flow Control Method for Airfoil Performance Enhancement Using Co-Flow Jet." *Applications of Circulation Control Technologies*, Chapter 10, p. 293-314, Vol. 214, Progress in Astronautics and Aeronautics, AIAA Book Series, Editors: Joslin, R. D. and Jones, G.S., 2006.

[4] G.-C. Zha, C. Paxton, A. Conley, A. Wells, and B. Carroll, "Effect of Injection Slot Size on High Performance Co-Flow Jet Airfoil," *AIAA Journal of Aircraft*, vol. 43, 2006.

[5] G.-C. Zha, B. Carroll, C. Paxton, A. Conley, and A. Wells, "High Performance Airfoil with Co-Flow Jet Flow Control," *AIAA Journal*, vol. 45, 2007.

[6] Wang, B.-Y. and Haddoukessouni, B. and Levy, J. and Zha, G.-C., "Numerical Investigations of Injection Slot Size Effect on the Performance of Co-Flow Jet Airfoil ," *AIAA Journal of Aircraft*, vol. 45, pp. 2084–2091, 2008.

[7] B. P. E. Dano, D. Kirk, and G.-C. Zha, "Experimental Investigation of Jet Mixing Mechanism of Co- Flow Jet Airfoil." AIAA-2010-4421, 5th AIAA Flow Control Conference, Chicago, IL, 28 Jun - 1 Jul 2010.

[8] B. P. E. Dano, G.-C. Zha, and M. Castillo, "Experimental Study of Co-Flow Jet Airfoil Performance Enhancement Using Micro Discreet Jets." AIAA Paper 2011-0941, 49th AIAA Aerospace Sciences Meeting, Orlando, FL, 4-7 January 2011.

[9] Lefebvre, A. and Zha, G.-C. , "Design of High Wing Loading Compact Electric Airplane Utilizing Co-Flow Jet Flow Control." AIAA Paper 2015-0772, AIAA SciTech2015: 53nd Aerospace Sciences Meeting, Kissimmee, FL, 5-9 Jan 2015.

[10] Lefebvre, A. and Dano, B. and Bartow, W. and Di Franzo, M. and Zha, G.-C., "Performance Enhancement and Energy Expenditure of Co-Flow Jet Airfoil with Variation of Mach Number." AIAA Paper 2013-0490, AIAA Journal of Aircraft, DOI: 10.2514/1.C033113, 2016.

[11] Liu, Z.-X. and Zha, G.-C., "Transonic Airfoil Performance Enhancement Using Co-Flow Jet Active Flow Control." AIAA Paper 2016-3066, AIAA Aviation, June 13-17 2016.

[12] J. Boling, S. Dhakal, Y. Yang, and G. Zha, "Numerical investigation of low speed performance of transonic coflow jet airfoil," in *35th AIAA Applied Aerodynamics Conference*, p. 3249, 2017.

[13] P. R. Spalart and S. R. Allmaras, "A one-equation turbulence model for aerodynamic flows," in *30th Aerospace Sciences Meeting and Exhibit, Aerospace Sciences Meetings, Reno, NV, USA, AIAA Paper 92-0439*, 1992.

[14] Jameson, A., "Time Dependent Calculations Using Multigrid with Applications to Unsteady Flows Past Airfoils and Wings." AIAA Paper 91-1596, 1991.

[15] Zha, G.C., Shen, Y.Q. and Wang, B.Y., "An improved low diffusion E-CUSP upwind scheme ," *Journal of Computer and Fluids*, vol. 48, pp. 214–220, Sep. 2011.

[16] Edwards, J.R., "A Low-Diffusion Flux-Splitting Scheme for Navier-Stokes Calculations," *Computer & Fluids*, vol. 6, pp. 635–659,doi:10.1016/S0045–7930(97)00014–5, 1997.

[17] Shen, Y.Q., and Zha, G.C., "Improvement of the WENO Scheme Smoothness Estimator," *International Journal for Numerical Methods in Fluids*, vol. 64,, pp. 653–675, DOI:10.1002/fld.2186, 2009.

[18] Shen, Y.Q., Zha, G.C., and Wang, B.Y., "Improvement of Stability and Accuracy of Implicit WENO Scheme," *AIAA Journal*, vol. 47, pp. 331–334, DOI:10.2514/1.37697, 2009.

[19] Shen, Y.Q., and Zha, G.C., "Large Eddy Simulation Using a New Set of Sixth Order Schemes for Compressible Viscous Terms," *Journal of Computational Physics*, vol. 229, pp. 8296–8312, doi:10.1016/j.jcp.2010.07.017, 2010.

[20] Shen, Y.Q., Zha, G.C., and Chen, X., "High Order Conservative Differencing for Viscous Terms and the Application to Vortex-Induced Vibration Flows," *Journal of Computational Physics*, vol. 228(2), pp. 8283–8300, doi:10.1016/j.jcp.2009.08.004, 2009.

[21] Lefebvre, A. and Zha, G.-C., "Trade Study of 3D Co-Flow Jet Wing for Cruise Performance." AIAA Paper 2016-0570, AIAA SCITECH2016, AIAA Aerospace Science Meeting, San Diego, CA, 4-8 January 2016.